High-entropy spinel (FeCoNiMnAl)$_3$O$_4$ with three-dimensional microflower structure for stable seawater oxidation

Changrui Feng [a], Yifan Zhou [a], Meng Chen [a,c], Lina Zou [a,d], Xiumin Li [d], Xiaowei An [e], Qiang Zhao [f], Pairuzha Xiaokaiti [g], Abuliti Abudula [a,*], Kai Yan [h,*], Guoqing Guan [a,b,**]

[a] Graduate School of Science and Technology, Hirosaki University, 3-Bunkyocho, Hirosaki 036-8561, Japan
[b] Energy Conversion Engineering Laboratory, Institute of Regional Innovation, Hirosaki University, 3-Bunkyocho, Hirosaki 036-8561, Japan
[c] College of Chemistry and Chemical Engineering, Xi`an University of Science and Technology, Xi`an 710054, China
[d] Zhengzhou University, Kexue Avenue 100, Zhengzhou, Henan 450001, China
[e] College of Environmental Science and Engineering, Taiyuan University of Technology, Taiyuan 030024, China
[f] School of Chemistry and Environmental Engineering, Shanxi Datong University, Datong 037009, China
[g] Frontier Laboratories Ltd., Fukushima 963-8862, Japan
[h] School of Environmental Science and Engineering, Sun Yat-sen University, Guangzhou 510275, China

ARTICLE INFO

ABSTRACT

In this study, high-entropy spinel (FeCoNiMnAl)$_3$O$_4$ catalyst with a three-dimensional(3D) layered microflower structure assembled by nanosheets grown on Ni foam (NF) is synthesized for stable seawater oxidation. Density functional theory (DFT) calculations indicate that it has a strong charge transfer capability, thereby reducing the energy barrier and boosting the reaction. As a result, a low oxygen evolution reaction (OER) overpotential of 274 mV@50 mA cm^{-2} is achieved with a small Tafel slope of 47.79 mV dec^{-1} in 1 M KOH solution. Notably, DFT calculations further verify that it shows stronger adsorption of OH$^-$ than Cl$^-$. As expected, the required overpotentials are still as low as 284 and 295 mV@50 mA cm^{-2} in alkaline simulated seawater and natural seawater electrolytes. Also, it exhibits excellent stability and corrosion resistance, maintaining stable OER activity over 50 h at 500 mA cm^{-2} in alkaline natural seawater, which has the potential to realize industrial electrochemical seawater splitting.

1. Introduction

At present, hydrogen production through water electrolysis is one of the most essential methods of green hydrogen production, which is characterized by its green and environmentally friendly nature, production flexibility, and high product purity [1–4]. In particular, it is the primary direction for hydrogen production from renewable energy sources such as photovoltaics and wind power. However, relying on freshwater electrolysis has placed even greater pressure on already scarce freshwater resources [5,6]. Oceans cover a major part (ca. 71%) of the Earth and seawater occupies about 97% of water resources in the world [7,8]. As a result, seawater electrolysis could become an attractive strategy to supersede water for hydrogen production. Moreover, hydrogen generated as fuel can further produce freshwater for seawater

purification. Despite the attractive advantages mentioned above, the complex composition of seawater brings about many challenges that need to be overcome for seawater electrolysis. Firstly, the existence of chloride ions (Cl$^-$, ~ 0.5 M) with a high concentration leads to the competition of chlorine evolution reaction (CER) with oxygen evolution reaction (OER) [9,10]. In order to inhibit the occurrence of CER, the electrocatalyst should possess high catalytic activity and selectivity since the difference of potentials between OER and CER is only 490 mV under alkaline conditions (pH > 7.5) and decreased with the pH reducing [11,12]. The second is severe electrode corrosion from Cl$^-$, which can damage the reactive sites and reduce the service life as well as the stability of catalysts [13,14]. Besides, calcium (Ca^{2+}) and magnesium ions (Mg^{2+}) are prone to forming insoluble hydroxide precipitations at high pH electrolytes. These insoluble precipitates not only

---

cover the electrode surface, thereby hindering effective contact between the catalyst and the electrolyte, but also block catalytic active sites, causing catalyst poisoning [15,16]. As a result, the fabrication of anodic catalysts with high selectivity, outstanding corrosion resistance and more active sites is the primary requirement for achieving efficient seawater electrolysis.

High-entropy materials (HEMs) have attracted great attention in the field of catalysis due to their intrinsic unique properties that unlike conventional composites [17–19]. The term "high-entropy" reflects the unusually high degree of disorder or entropy in the atomic arrangement, which can lead to unexpected and advantageous material characteristics. The most well-known aspect is their four core effects [20,21]. First is the high entropy effect by the entropy increase due to the random arrangement of all metal elements in the HEMs, which can lead to the HEMs being more inclined to form a single phase, which consistently exhibits the increased resistance to deformation, the improved strength, and, in some cases, unique electronic, magnetic, or catalytic properties [22]. The lattice distortion effect has resulted from the difference in atomic radii of elements that lead to asymmetric bonding structures and electron distributions. The thermodynamically non-equilibrium state resulting from this may especially lower the energy barriers for molecule adsorption, activation, and conversion in electrocatalytic reactions [23,24]. Compared with conventional metal composites, HEMs exhibit slower phase transformation and diffusion kinetics, which enhances chemical, thermal, and mechanical stability [25]. The "cocktail effects" of HEMs mainly refer to the synergistic effect of multiple components that can effectively optimize the intermediates' adsorption energy. As such, HEMs could be promising candidates applied for seawater electrolysis. In particular, the continuously distributed binding energy of HEMs can form active sites with ideal binding energies, and the intrinsic chemical and mechanical stability are conducive to resisting Cl^- corrosion [26].

It is found that transition metal oxides (TMOs) usually exhibit greater durability and higher stability but sometimes with relatively lower catalytic activity than those noble metal-based ones [27,28]. Recently, spinel oxides, a class of metal oxides with the general formula of AB_2O_4 characterized by the arrangement of oxygen ions in a cubic close-packed lattice with divalent cations on tetrahedral sites and trivalent cations on octahedral sites [29], have exhibited excellent promise for the application in energy conversion due to their unique electronic configurations, manifold compositions, and valence states [30–32]. The tuneable composition and geometrical configuration especially endow spinel oxides with a grear extent to be adjusted with more excellent performance toward OER electrocatalysis [33,34]. In this work, the high-entropy concept was introduced to fabricate a highly active high-entropy spinel oxide for stable seawater oxidation. Considering the abundance, high catalytic activity and compatibility with different electrode materials, Fe, Co and Ni were selected as the fundamental components [35], and then Mn and Al were introduced to modulate the electronic structure to promote the OER performance. The as-synthesized $(FeCoNiMnAl)_3O_4$ exhibited a three-dimensional (3D) layered microflower shape assembled from a large number of nanosheets, which effectively enlarged the surface area and cavities formed between nanosheets for mass transfer and gas release. Combining experimental and theoretical computational results, it is confirmed that introducing Al can decrease the energy barrier. Meanwhile, it is found that the Mn-containing high-entropy $(FeCoNiMnAl)_3O_4$ exhibited better performance than the prepared quaternary metal oxides, indicating the synergistic effect for the enhancement of intrinsic OER activity. Moreover, the high-entropy electrocatalyst showed stronger adsorption of Cl^- than other counterparts, but it can still relatively preferentially adsorb OH^-, thus endowing it with excellent OER selectivity. As a result, the as-synthesized $(FeCoNiMnAl)_3O_4$ electrocatalyst demonstrated low overpotentials of 274 and 295 mV@50 mA cm^{-2} for anodic OER, respectively in alkaline freshwater and natural seawater electrolytes. Especially, even at an industrial-level high current density of

500 mA cm^{-2} for seawater oxidation, it still maintained stable OER activity over 50 hours, whose excellent stability and corrosion resistance made it promising to realize industrial seawater electrolysis.

2. Experimental

2.1. Chemicals and materials

Fe(NO$_3$)$_3$·9 H$_2$O, Co(NO$_3$)$_2$·9 H$_2$O, Ni(NO$_3$)$_2$·6 H$_2$O, Al(NO$_3$)$_3$·6 H$_2$O, urea, NH$_4$F and ethanol (99.5%) were purchased from Wako, Japan. Mn (NO$_3$)$_2$·4 H$_2$O, RuO$_2$ and 5 wt% Nafion perfluorinated resin solution in aqueous aliphatic alcohol were provided by Sigma-Aldrich. The distilled water is produced from the ADVANTEC RFD240NC distilled water manufacturing equipment. The nickel foam (NF) with 11 pores per inch, a bulk density of 0.23 g/cm^3 and a thickness of 1.5 mm was bought from MTI, Japan. Natural seawater from the sea around north Japan (Fig. S15).

2.2. Fabrication of electrocatalyst coated electrode

In-situ growing of high-entropy $(FeCoNiMnAl)_3O_4$ on the NF included a hydrothermal process and a following annealing treatment step. Firstly, the NF was pre-treated with HCl to clean out those metal oxides and impurities. In brief, the NF with a dimension of 2×2 cm^2 in the 3 M HCl solution was treated by ultrasonication for 30 min, and then washed with distilled water and ethanol in turn for several times followed by drying in a vacuum at 60 °C for further use. For the hydrothermal process, Fe(NO$_3$)$_3$·9 H$_2$O (10 mM), Co(NO$_3$)$_2$·6 H$_2$O (20 mM), Ni(NO$_3$)$_2$·6 H$_2$O (20 mM), Mn(NO$_3$)$_2$·4 H$_2$O (25 mM) and Al (NO$_3$)$_3$·6 H$_2$O (10 mM) were mixed with NH$_4$F (170 mM) and urea (340 mM) to obtain a clear pink solution under continuous magnetic stirring for 30 min. Then, the solution was introduced into a 50 mL autoclave with the addition of the pretreated NF for hydrothermal reaction at 140 °C for 16 hours to prepare FeCoNiMnAl hydroxide precursor. After the hydrothermal process, the catalyst precursor coated NF was washed for several times with ethanol and dried in the vacuum at 60 °C for 12 h. After that, the electrode was annealed in a furnace at 350 °C for 2 hours (heating rate: 2 °C/min) to obtain the high-entropy (FeCoNiMnAl)$_3$O$_4$ oxide. For comparison, the corresponding (FeCoNi)$_3$O$_4$, (FeCoNiMn)$_3$O$_4$ and (FeCoNiAl)$_3$O$_4$ were also coated on the pretreated NF sheets under the same conditions only only in the absences of the absent nitrate salts.

2.3. Characterizations of electrocatalysts

Scanning electron microscope (JEOL JSM-7000 F type SEM working at 10 kV) and transmission electron microscopy (JEOL JEM-2100 type TEM working at 200 kV) were applied to characterize the morphology and nanostructure of the as-fabricated catalysts, respectively. The amounts of metal species in the catalysts were further determined by ICP-OES (i.e., Inductively Coupled Plasma Optical Emission Spectrometry). To confirm crystal structure of the as-synthesized catalyst, an X-ray powder diffractor (XRD, Rigaku Smartlab) with the Cu-Kα radiation source was used in a 2θ range of $10°-90°$. Raman spectrum was measured by a Jasco NRS-5500 type laser Raman spectrophotometer (exciting wavelength: 532 nm). X-ray photoelectron spectrum (XPS) was detected using a VG Scientific ESCALab250i-XL equipment for each element in the catalyst.

2.4. Electrochemical measurements

Electrochemical performance was evaluated by a three-electrode system, in which a graphite rod with a diameter of 6 mm was applied as the counter electrode and a standar Hg/HgO electrode was used as the reference electrode on a VersaSTAT4 electrochemical workstation (Princeton, USA). Electrochemical activation was firstly proceeded

before OER test through cyclic voltammetry (CV) measurement with 50 mV s^{-1} (Potential range: 0–1.5 V (vs Hg/HgO)). After the CV curve became stable, LSV was tested in the same potential range at 2 mV s^{-1}. The LSV results were corrected with 95% iR compensation through manual correction method and the final potential was calculated as E $_{(vs\ RHE)}$ = E $_{(vs\ Hg/HgO)}$ + 0.059 pH + E$_{Hg/HgO}$ − 95%iR_s. EIS test for charge transfer resistance (R$_{ct}$) was conducted at 314 mV in a frequency range of 100 kHz~0.01 Hz. The electrochemical surface area (ECSA) was obtained by the measured CV curves in a non-Faradic region of 0 ~ 0.1 V (vs Hg/HgO) at various scan rates of 10, 15, 20, 25, 30 mV s^{-1}. Furthermore, a multi-step chronopotentiometry was tested in 1 M KOH at 50, 100, 200, 300, 400 and 500 mA cm^{-2} with a time interval of 1 hour. The long-term durability of the as-fabricated electrode was tested by the chronopotentiometry at an industrial-level current density of 500 mA cm^{-2} for 50 hours in 1 M KOH, 1 M KOH + 0.5 M NaCl, or 1 M KOH + seawater. The experiment on hypochlorite species (ClO$^-$) detection after stability test is shown in Supplementary Material.

2.5. Density functional theory (DFT) calculations

All DFT calculations were conducted with an all-electron method implemented in DMol3. The electron exchange-correlation functions of the generalized gradient approximation (GGA) and Perdew-Burke-Ernzerhof (PBE), along with a double numerical plus polarization (DNP) basis set, were employed for these calculations. The k points were set at 5×5×1 using the Monkhorst-Pack method. The lattice parameter in the *z* direction was fixed with a vacuum width of 15 Å, whereas the lattice parameters in the *x* and *y* directions exceeded 14 Å to prevent spurious interactions between repeating slabs effectively. Lattice parameters in the *x-y* plane and atom coordinates were permitted to undergo full relaxation.

3. Results and discussion

3.1. Synthesis and characterization of the (FeCoNiMnAl)$_3$O$_4$

The fabrication process of high-entropy (FeCoNiMnAl)$_3$O$_4$ on NF ((FeCoNiMnAl)$_3$O$_4$/NF) is illustrated in Fig. 1. The FeCoNiMnAl precursor with an orange color is first covered on NF by a hydrothermal process. After it is treated at 350 °C in air for 2 h, the (FeCoNiMnAl)$_3$O$_4$/NF electrode with the color change from orange to black (Fig. S1) is obtained. From SEM image at lower magnification, the as-synthesized (FeCoNiMnAl)$_3$O$_4$ particles with a microflower-like shape are distributed uniformly and compactly around the surface of NF with an average particle size of 3.90 ± 1.44 μm (Fig. 2a, b, S3). The morphology with a higher magnification clearly exhibits a 3D layered microflower structure assembled by a large number of nanosheets (Fig. 2c). This specific

structure could provide a larger surface area and more active sites. Moreover, those abundant cavities formed among the nanosheets benefit to mass transfer and gas release. The contact angle test further verifies that the catalyst layer possesses excellent hydrophilicity (Video S1), which not only ensures effective contact of catalyst with the electrolyte, but also is conducive to suppressing the formation of bubbles on the catalyst surface in the electrolysis process, thereby avoiding the gathering of bubbles on the surface to cover the active sites and the falling out of catalysts. Meanwhile, the XRD analysis was applied to confirm the crystalline structures of the synthesized catalysts. As demonstrated in Fig. 2d, the diffraction peaks of the catalyst well correspond to the face-centered cubic (FCC) spinel structure (JCPDS#20–0781), and the prominent peaks at 18.78°, 31.06°, 36.16°, 37.92°, 44.02°, 58.10° and 64.08° are attributed to (111), (220), (311), (222), (400), (511), (440) crystal planes, respectively. ICP-OES was further tested to determine the exact atomic ratio of all metal elements, by which all atomic ratios are in the range of 5 ~ 35% (Fig. S4), which is in accordance with the definition of high-entropy materials. Consequently, by combining the results from XRD and ICP-OES analyses, the as-synthesized (FeCoNiMnAl)$_3$O$_4$ is proved to be a high-entropy metal oxide with a spinel structure. TEM characterization was further used to confirm the nanostructure and crystalline structure. As shown in Fig. 2f, the edges of the nanosheets are found to have many nanopores that can further enlarge the surface area. The two main lattice fringes on the HRTEM image with crystalline interplanar spacings of 0.284 and 0.241 nm are well matched with the (220) and (311) lattice planes of the spinel structure (Fig. 2g and h). These results are also supported by the selected-area electron diffraction (SAED) as shown in Fig. 2i, in which the characterization of concentric rings with contrast bright spots indicates the polycrystalline nature of (FeCoNiMnAl)$_3$O$_4$, and the radius of the concentric rings measured manifested that they are associated to (220), (311), (400), (422), (511) and (440) planes of the spinel crystal phase respectively. Such HRTEM and SAED patterns firmly support the results of XRD analysis, confirming that the as-synthesized (FeCoNiMnAl)$_3$O$_4$ should be a single-phase spinel. Meanwhile, the corresponding element mappings (Fig. 2j) confirm the fine elemental distributions. Raman analysis was further used to verify the spinel structure. As shown in Fig. 3a, the Raman spectrum of (FeCoNiMnAl)$_3$O$_4$ has four characteristic peaks at 173, 517, 610 and 644 cm^{-1}, relating to the F$_{2\ g}$, F$_{2\ g}$, F$_{2\ g}$ and A$_{1\ g}$ vibrational modes of the spinel structure, respectively, which are related to the high-entropy metal oxide (detail information on peaks is summarized in Table S1) [36,37].

Surface chemical states and electronic interactions of the high-entropy (FeCoNiMnAl)$_3$O$_4$ metal oxide and the counterparts (i.e., (FeCoNiMn)$_3$O$_4$, (FeCoNiAl)$_3$O$_4$, (FeCoNi)$_3$O$_4$) were analyzed through XPS. Fig. 3b demonstrates the wide range spectra of the as-synthesized catalysts; the presence of corresponding peaks reflects the existence of

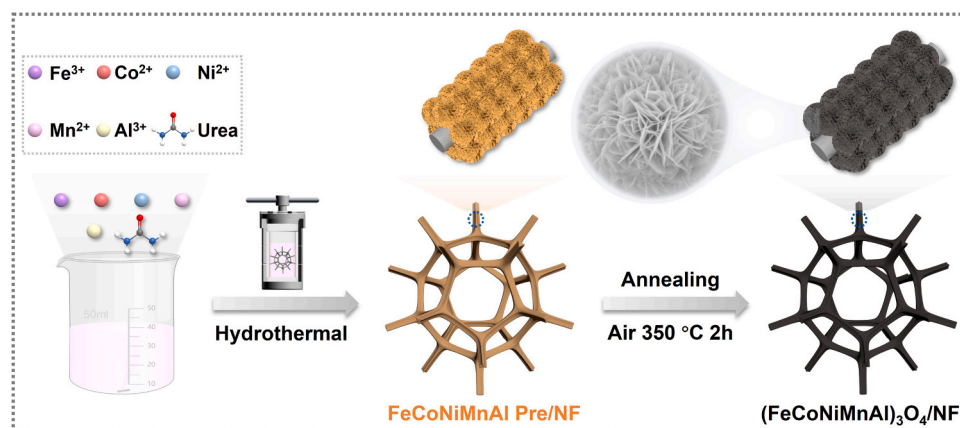**Fig. 1.** Schematic illustration of the synthesis process for 3D layered microflower-shape (FeCoNiMnAl)$_3$O$_4$ grown on the Ni foam.
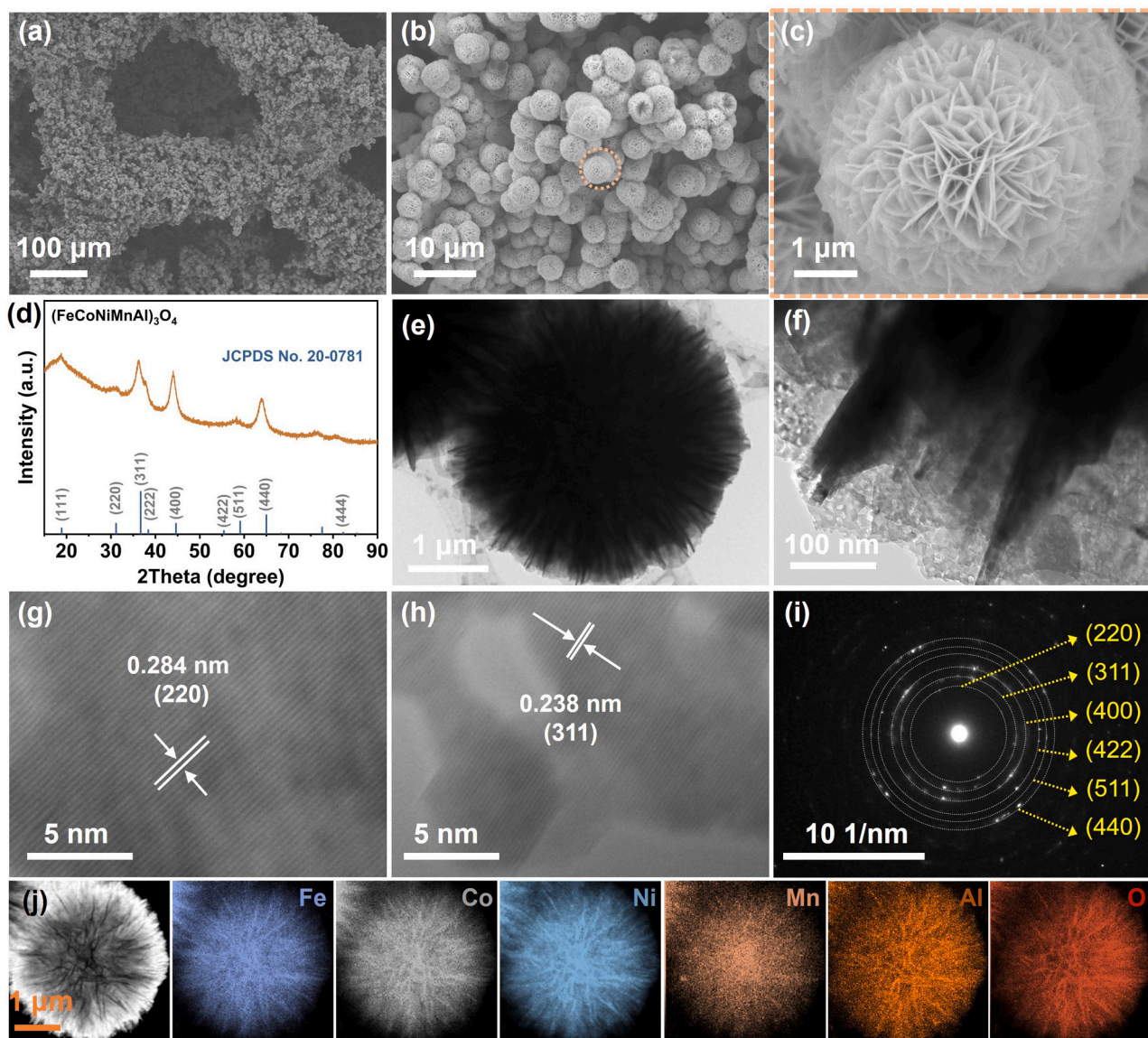
Fig. 2. Morphology, nanostructure and elemental distributions of the synthesized catalyst. (a-c) SEM, (d) XRD, (e, f) TEM, (g, h) HRTEM, (i) SAED pattern and (j) EDS elemental mappings of $(FeCoNiMnAl)_3O_4$.

Fe, Co, Ni, Mn, Al and O element, which correspond to the EDS analysis results. As shown in Fig. 3**c**, the high-resolution XPS spectrum of Fe 2p can be divided into three peaks, corresponding to three valence states, including Fe^0, Fe^{2+} and Fe^{3+}, which are located at 705.96/719.75, 711.03/723.83, 713.81/727.44 eV, respectively [38]. As for Co 2p, the appeared one pair of spin-orbit doublets at 780.46 and 796.02 eV is belonged to Co^{3+}, and another pair of doublets at higher binding energy situated at 783.00 and 798.79 eV is attributed to Co^{2+} (Fig. 3**d**) [39]. The XPS spectrum of Ni 2p (Fig. 3**e**) is composed of $2p_{1/2}$, $2p_{3/2}$ doublets and two satellite peaks, in which two peaks at 855.06 (Ni $2p_{3/2}$) and 872.24 eV (Ni $2p_{1/2}$) can be assigned to Ni^{2+} while the adjacent two peaks located at 856.72 and 874.86 eV are pertained to Ni^{3+}. Besides, two shake-up satellite peaks are also observed at 645.11/657.46 eV [40]. Compared with $(FeCoNi)_3O_4$, the peaks of Fe 2p, Co 2p and Ni 2p all shift towards the higher binding energy after MnAl-addition, demonstrating the occurrence of electron transfer between these metal elements. The high-resolution Mn 2p XPS spectra of $(FeCoNiMnAl)_3O_4$ and $(FeCoNiMn)_3O_4$ are displayed in Fig. 3**f**. Here, the profile of the Mn $2p_{3/2}$ spectrum is split into three peaks, suggesting three states of Mn species on the catalyst surface, where the binding energies at 637.42,

639.56 and 641.65 eV are assigned to Mn^{2+}, Mn^{3+} and Mn^{4+}, respectively [41,42]. It is obvious to observe that the Mn 2p peaks show positive shifts when comparing the high-entropy $(FeCoNiMnAl)_3O_4$ with the quaternary $(FeCoNiAl)_3O_4$ metal oxide, indicating that the electron density around Mn is decreased since it can serve as the electron donor in the catalyst. In addition, Fig. 3**g** displays high-resolution XPS spectrum of Al 2p, in which the peak at 73.63 eV is attributed to AlO_X [43]. In the existence of Mn, the peak position of AlO_X is shifted by 0.18 eV to the lower binding energy, indicating electron transfer from other metal elements to Al. The XPS spectrum of O 2 s in Fig. 3**h** shows three kinds of O species, corresponding to lattice oxygen (O_L, 529.98 eV), oxygen vacancy (O_V, 531.73 eV) and surface adsorption water (O_W, 533.05 eV) [44]. Here, the important role of O vacancy in catalysis should be noticeable since it has been reported to contribute to electron transport and enhance electrochemical performance. Therefore, the proportion of O_V was further calculated based on the peak area, and it is found that its ratios are 27.67% and 54.98% for $(FeCoNi)_3O_4$ and $(FeCoNiMnAl)_3O_4$, respectively. The apparent higher ratio manifests that more O vacancies are formed on the high-entropy $(FeCoNiMnAl)_3O_4$ surface, and the same trend was also confirmed by EPR (Fig. 3**i**). Obviously, the high-entropy
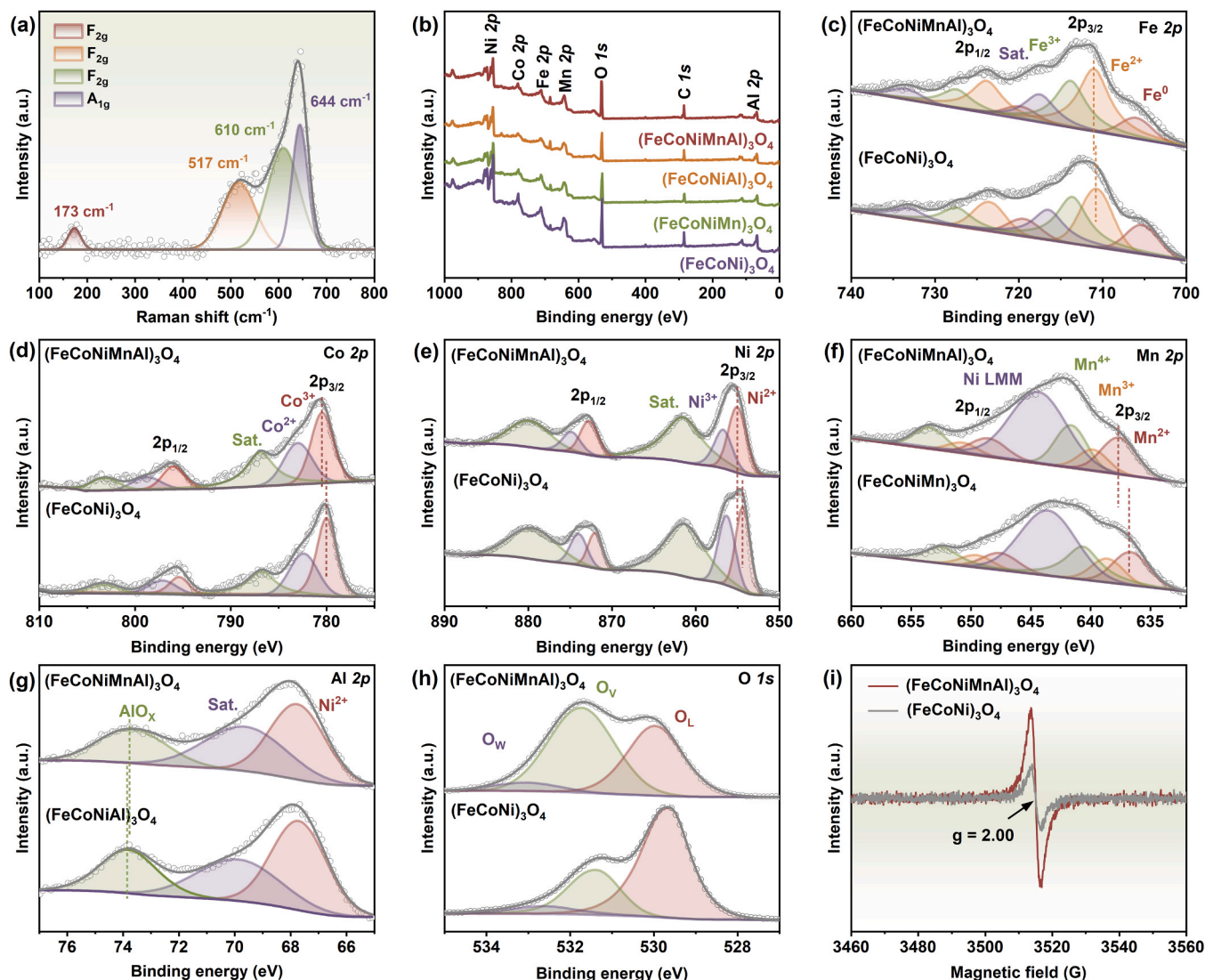
Fig. 3. Raman, XPS and EPR analysis. (a) Raman spectrum of $(FeCoNiMnAl)_3O_4$; (b) Full XPS spectrum; and high-resolution XPS spectra of (c) Fe 2p, (d) Co 2p, (e) Ni 2p, (f) Mn 2p, (g) Al 2p and (h) O 1 s. (i) EPR spectra of different catalysts.

$(FeCoNiMnAl)_3O_4$ gives a stronger magnetic signal than the $(FeCoNi)_3O_4$, which demonstrates a higher concentration of unpaired electrons resulted from the oxygen defects [45]. Based on the XPS and EPR analysis results above, it can be concluded that the high-entropy $(FeCoNiMnAl)_3O_4$ catalyst should have strong electronic interaction, which is conducive to optimizing the electric structure. Moreover, the rich oxygen defects could also lead to the positive effect on the electrocatalytic performance [46].

3.2. OER performance of $(FeCoNiMnAl)_3O_4$

Firstly, OER activities of as-prepared electrodes were tested in freshwater-based 1 M KOH solution. Fig. 4a provides superposition LSV curves of as-fabricated $(FeCoNiMnAl)_3O_4$, $(FeCoNiAl)_3O_4$, $(FeCoNiMn)_3O_4$, $(FeCoNi)_3O_4$ and commercial RuO_2 based electrodes with 95% iR correction. The LSV curve of $(FeCoNiMnAl)_3O_4$ (I) is the steepest, and as summarized in Fig. 4b, it requires an ultra-low overpotential of 274 mV to reach a high current density of 50 mA cm^{-2}, which is superior to those of quaternary $(FeCoNiAl)_3O_4$ (II, 309 mV), $(FeCoNiMn)_3O_4$ (III, 359 mV), ternary $(FeCoNi)_3O_4$ (IV, 340 mV), and even commercial RuO_2 (V, 391 mV). Besides, the OER performance of this high-entropy $(FeCoNiMnAl)_3O_4$ also locates the ahead of those reported

electrocatalysts as shown in Table S2. A very interesting phenomenon that occurred here is that the OER activity is abnormally reduced slightly after the introduction of Mn, which may be due to MnOx not playing a catalytically active function in this catalyst. Subsequently, the reaction kinetics were assessed through the linear fitted Tafel slopes (Fig. 4c). The lower Tafel slope of high-entropy $(FeCoNiMnAl)_3O_4$ (40.13 mV dec^{-1}) compared with $(FeCoNiAl)_3O_4$ (73.37 mV dec^{-1}), $(FeCoNiMn)_3O_4$ (89.57 mV dec^{-1}), $(FeCoNi)_3O_4$ (97.06 mV dec^{-1}) and RuO_2 (104.93 mV dec^{-1}) indicates that a faster reaction kinetics of OER can occur on this high-entropy catalyst. Cyclic voltammetry curves were measured under various scan rates to obtain electrochemical double layer capacitances (C_{dl}). As displayed in Fig. 4d, the fitted C_{dl} of high-entropy $(FeCoNiMnAl)_3O_4$ is 32.87 mF cm^{-2}, which is also higher than those corresponded trinary and quaternary metal oxides, indicating that the formation of high-entropy compound has created more active sites for OER. Electrochemical impedance spectroscopy (EIS) analysis was conducted for the assessment of charge transfer kinetics. As demonstrated in Fig. 4e, the fitted semicircle diameter of high-entropy $(FeCoNiMnAl)_3O_4$ is smaller than the counterparts with the charge transfer resistance (R_{ct}) value of 0.56 Ω, which is much lower than those of $(FeCoNi)_3O_4$ (1.97 Ω), $(FeCoNiMn)_3O_4$ (2.28 Ω) and $(FeCoNiAl)_3O_4$ (1.02 Ω). Thus, the $(FeCoNiMnAl)_3O_4$ should possess faster charge
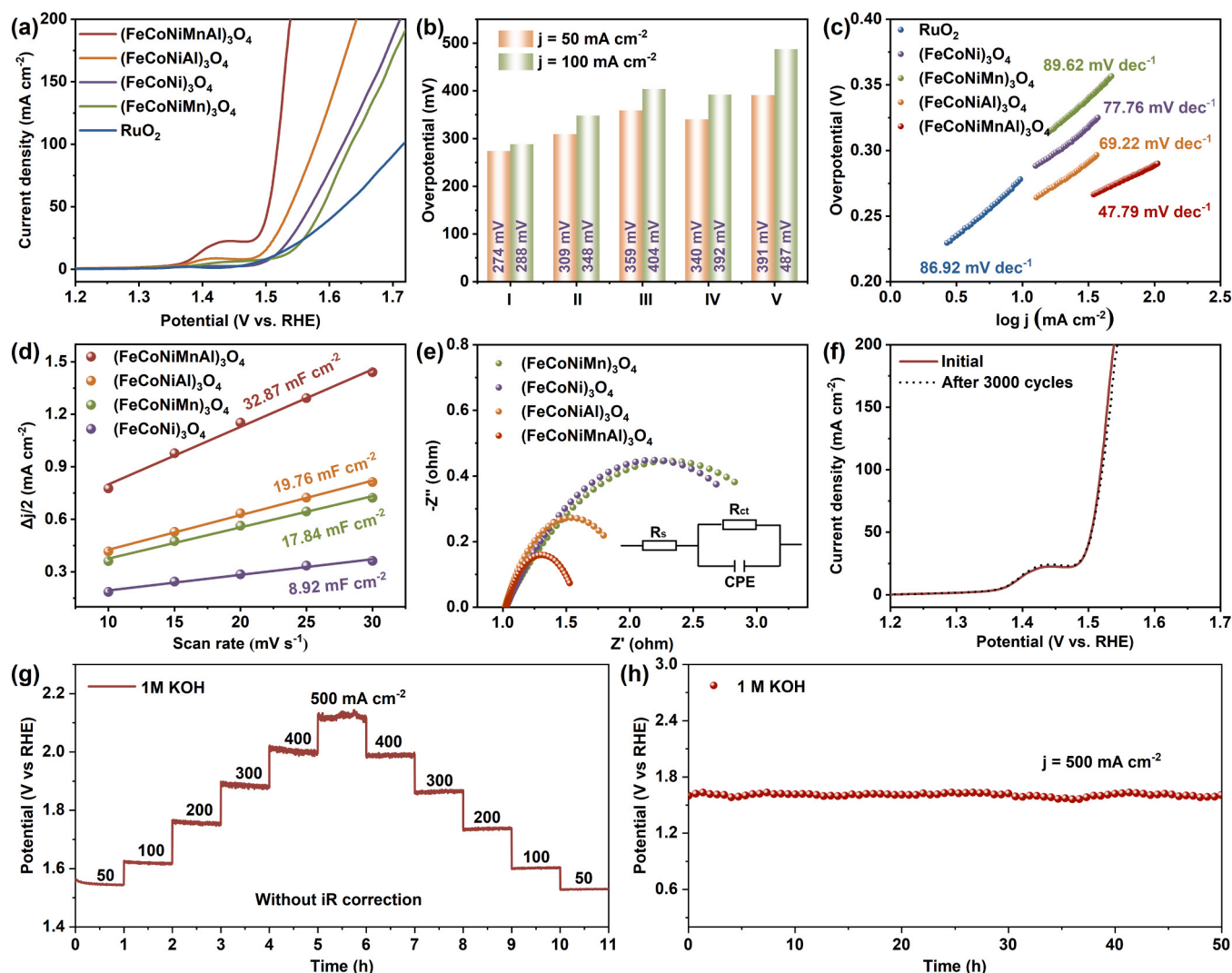
Fig. 4. Electrochemical performance in freshwater based electrolyte with 1 M KOH. (a) OER curves; (b) overpotentials at different current densities; (c) Tafel plots; (d) double layer capacitance; (e) EIS; (f) polarizations before and after 3000 cycles; (g) stepped chronoamperometric curve; and (h) chronoamperometric curve at a high constant current density of 500 mA cm^{-2}.

transfer capability, which is conducive to enhancing OER. In addition to the OER activity investigation of the as-prepared catalyst, the long-term stability exploration of the high-entropy (FeCoNiMnAl)$_3$O$_4$ was also performed. As shown in Fig. 4**f**, the polarization curve after 3000 cycles of testing is still basically consistent with the initial one. Moreover, the chronopotentiometry was employed to obtain the multi-step CP curve under different current densities varied from 50 to 500 mA cm^{-2} and eventually returning to 50 mA cm^{-2} (Fig. 4**g**). It can be found that the potential makes sensitive changes accordingly as the current density rises or falls in a stepwise manner, which indicates that the catalyst has excellent mass and electron transfer properties. What's more, the potential remains stable throughout the set one-hour interval for each step (decay/increase ≤ 1.25%), manifesting the excellent stability of the high-entropy catalyst under different current densities. Besides, the long-term stability was also evaluated on account of its vital role in actual electrolysis application. As demonstrated in Fig. 4**h**, the potential does not show significant fluctuations even at an industrial-level high current density of 500 mA cm^{-2} for a continuous 50-h OER test. In conclusion, the as-fabricated high-entropy (FeCoNiMnAl)$_3$O$_4$ possesses excellent OER catalytic activity as well as impressive mechanical stability in alkaline freshwater electrolytes.

3.3. OER performance for seawater electrolysis

Due to the impressive catalytic performance of the high-entropy (FeCoNiMnAl)$_3$O$_4$ in alkaline freshwater-based (1 M KOH) electrolyte, its OER activity in seawater electrolyte was further investigated. Here, the alkaline simulated seawater (1 M KOH + 0.5 M NaCl) and alkaline natural seawater (1 M KOH + Seawater) serve as the electrolytes for tests. As demonstrated in Fig. 5**a**, comparing with the freshwater electrolysis, the catalytic activities all decrease under these hasher corrosive conditions. The required overpotentials are 284 and 304 mV at current densities of 50 and 100 mA cm^{-2}, respectively, in the alkaline simulated seawater electrolyte. The activity reduction may be ascribed to the presence of high concentration Cl$^-$ that interferes with or even poisons the catalyst. While, the further decay of OER performance (η_{50} = 295 mV) in the natural seawater electrolysis could be due to the fact that the existing Ca^{2+} and Mg^{2+} in the natural seawater can form insoluble precipitates under alkaline conditions, which could cover the active sites of the catalyst. The faradic efficiency (FE) in 1 M KOH + seawater was also determined by a drainage method at a constant current density of 50 mA cm^{-2} (Fig. 5**c**, **S17**), which is around 97.2%, demonstrating the high OER selectivity of this high-entropy oxide catalyst. As for seawater electrolysis, the corrosion resistance performance of the catalyst needs to be taken into account for the application. Thus, the corrosion
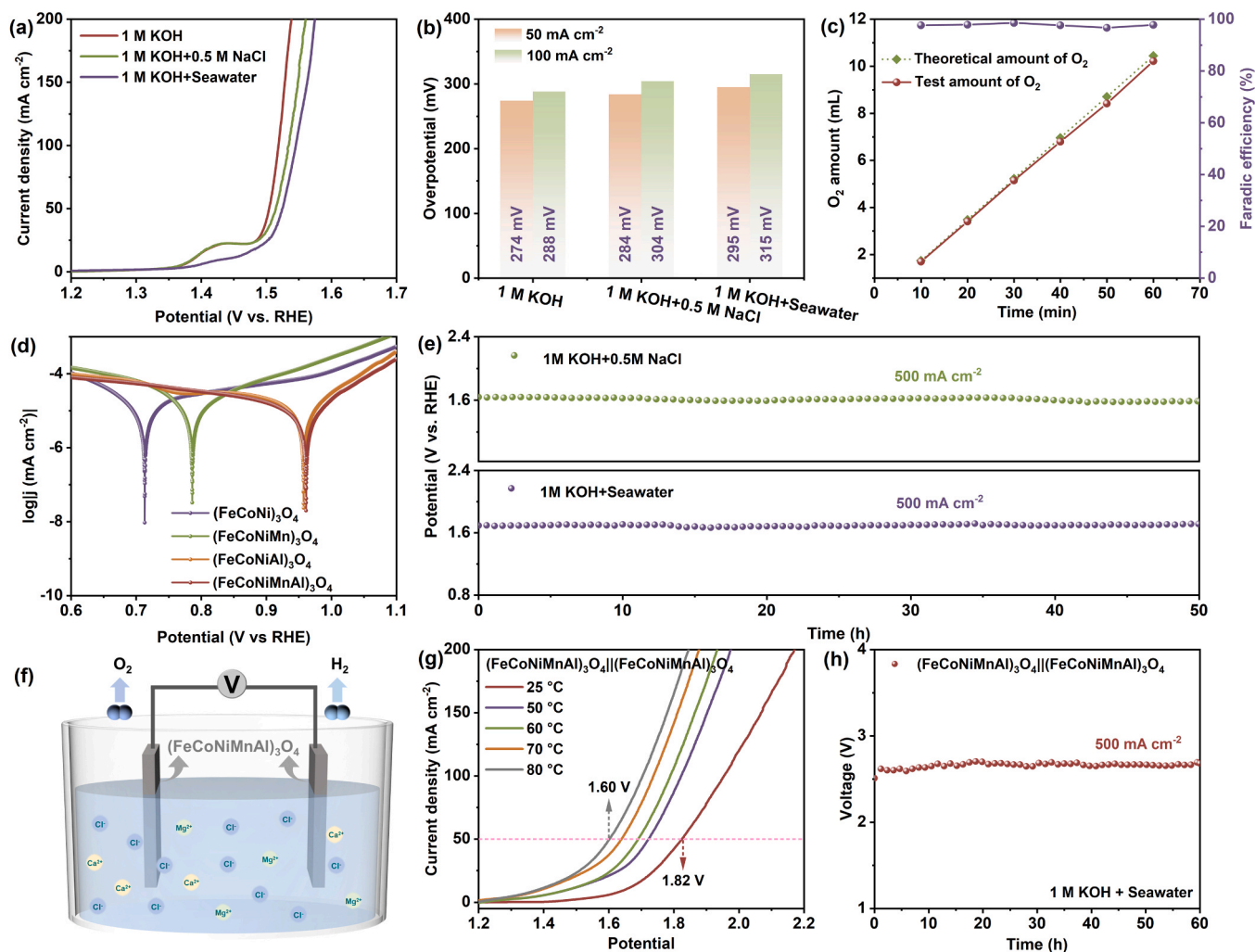
Fig. 5. Electrocatalytic performance in seawater based electrolyte. (a) Polarization curves and (b) overpotentials in different electrolytes; (c) The collected (red) and theoretical (green) oxygen volume in 1 M KOH + seawater electrolyte at the current density of 100 mA cm^{-2}; (d) Corrosive curves of different catalysts in natural seawater; (e) Stability test under 500 mA cm^{-2} in 1 M KOH + 0.5 M NaCl and 1 M KOH + seawater solutions; (h) Schematic illustration of overall seawater splitting by using (FeCoNiMnAl)$_3$O$_4$ as the bifunctional electrocatalysts for both cathode and anode; (g) Polarization curves of overall seawater spitting under different temperatures; (h) Chrono potentiometric curve at 500 mA cm^{-2} for 60-h stability test.

resistance of high-entropy (FeCoNiMnAl)3O4 was subsequently evaluated in natural seawater through Tafel corrosion polarization analysis. As shown in Fig. 5d, the high-entropy (FeCoNiMnAl)$_3$O$_4$ catalyst exhibits lower corrosion current (I$_{corr}$) and higher corrosion potential (E$_{corr}$) compared with the counterparts, which indicates high corrosion resistance of as-prepared high-entropy catalyst (Fig. S18). Finally, the stability test was carried out in simulated seawater and natural seawater based electrolytes separately. As displayed in Fig. 5e, the high-entropy (FeCoNiMnAl)$_3$O$_4$ exhibits superior long-term durability for 50 h continuous operating in both of the above electrolytes even at an industrial-level high current density of 500 mA cm^{-2}. Then DPD (N, N-diethyl-p-phenylenediamine) reagents were used as indicators with UV–vis spectrophotometry method to verify whether hypochlorite was generated in alkaline seawater solution [47–49]. Based on the color-reaction mechanism of the DPD as the indicator, at the pH range of 6.2 ~ 6.5, DPD will be directly oxidized when there is hypochlorite species present and produce a magenta-colored compound (Fig. S19a). Besides, the absorption peaks will appear at ~ 510 nm and ~ 551 nm when it is detected using UV spectroscopy. As demonstrated in Fig. S19b, it can be observed that in the presence of NaClO, the solution exhibits a pale pink color, and distinct absorption peaks appear at 510 and 551 nm in the UV–vis analysis results. However, the phosphate

buffer solution and the electrolyte solution after OER remain clear and transparent without UV absorption peaks observed (Fig. S19c), indicating that no hypochlorite species are formed in the electrolyte.

HER performance of high-entropy (FeCoNiMnAl)$_3$O$_4$ was also explored in alkaline natural seawater. As derived from the polarization curve in Fig. S20, the overpotential value at 50 mA cm^{-2} is 185 mV. Benefiting from the excellent OER and HER activities, the high-entropy catalyst applied as the bifunctional electrocatalysts for overall seawater electrolysis was also investigated. It is found that the required voltage to achieve the current density of 50 mA cm^{-2} is 1.82 V without iR correction. As for industrial water splitting, the operating temperature is usually in the range of 50–80 °C. Therefore, the overall electrolysis performance was also evaluated at the above temperature range and the obtained polarization curves are illustrated in Fig. 5g. One can see that the catalytic activity gradually increases as temperature rises. As the temperature of the electrolyte solution reaches 80 °C, the needed voltage to achieve 50 mA cm^{-2} is reduced to as low as 1.60 V. The assembled two-electrode electrolyzer also can maintain outstanding performance without noticeable degradation for over 60-h electrolysis at the high constant current density of 500 mA cm^{-2} (Fig. 5h). The morphology and structure transformation were also investigated after long-term stability test in natural seawater based electrolyte. As demonstrated in

Figs. S21a-c, the overall morphology of the catalyst primarily remains unchanged even on a microscopic scale. Besides, the lattice fringes obtained from HRTEM still clearly give two interplanar spacings of 0.298 and 0.252 nm, which are in accordance with the (220) and (311) planes of spinel structure (**Figs. S21e** and **f**), indicating the outstanding structural stability and strong chlorine corrosion resistance of the as-synthesized high-entropy electrocatalyst. The elemental analysis further confirms the existence of all elements in the catalyst after the stability test (Fig. S21g). In the meantime, XPS analysis was employed to explore the change of element valence states in $(FeCoNiMnAl)_3O_4$. The wide-scan spectrum as displayed in Fig. S22 exhibits the corresponding XPS peaks of all elements included in the spent $(FeCoNiMnAl)_3O_4$. In contrast, the appearance of XPS peaks associated to Na, K and Cl is observed since the long-term stability testing leads to these ions absorbed on the catalyst surface. The high-resolution spectra (Fig. S23) were fitted to reveal the valence state changes and they remained the same as the fresh ones before OER test. Thus, it can be concluded that the high-entropy $(FeCoNiMnAl)_3O_4$ has excellent structural stability for seawater oxidation even at industrial-level high current density.

3.4. DFT calculation

DFT calculation was employed to reveal the relationship between OER performance as well as selectivity and the electronic structure on the catalyst surface [50]. The model was constructed based on the spinel structure from XRD result, and Ni site was used as the main reactive site for all calculations due to its higher content (Fig. S24). At first, the *d*-orbital partial density of states (*d*-PDOS) was calculated in order to understand the local electronic environment better. As demonstrated in Fig. 6a, the *d* orbital of Ni in $(FeCoNiMnAl)_3O_4$ has a higher charge carrier density near the Fermi level, indicating the stronger charge transfer ability of the high-entropy catalyst. Due to the catalytic performance is strongly associated with the adsorption energy of the reaction intermediates (i.e., *OH, *O and *OOH), here, the OER free energy was calculated and the diagram is displayed in Fig. 6b to show the energy barrier of each step. Whether for the high entropy catalyst or

the counterparts, the second step exhibits the highest energy barrier, which manifests that the dissociation of *OH for the formation of *O is dynamically unfavorable and thus, it is regarded as the rate-determine step. Specifically, for the trinary $(FeCoNi)_3O_4$, the free energy of the second step is 1.99 eV under standard conditions (U = 0 V). Meanwhile, the ΔG remains unchanged after the introduction of Mn, verifying that it does not play a catalytically active function as mentioned in the above discussion. Compared with $(FeCoNiAl)_3O_4$, for the high-entropy $(FeCoNiMnAl)_3O_4$ catalyst, the energy barrier is further reduced. Thus, the high-entropy catalyst should exhibit a strong synergistic effect to obtain the optimized OER performance, which is consistent with the experimental result. As the applied potential is increased to 1.23 V (U = 1.23 V), the reaction limited energy barrier of $(FeCoNiMnAl)_3O_4$ (0.61 eV) is still lower than those of $(FeCoNi)_3O_4$ (0.75 eV), $(FeCoNiMn)_3O_4$ (0.76 eV) and $(FeCoNiAl)_3O_4$ (0.66 eV), which demonstrates promoted OER kinetics. In addition, the adsorption of Cl^- and OH^- was also investigated to prove the OER selectivity [51]. As shown in Fig. 6e, the high-entropy $(FeCoNiMnAl)_3O_4$ shows a stronger adsorption capacity of Cl^-, which is not conducive to its further oxidation and thereby restraining CER. Besides, all samples exhibit stronger adsorptions of OH^- than Cl^- (Fig. 6f), which should be beneficial in preventing Cl^- corrosion and undesirable CER. Thus, as-synthesized catalysts can exhibit excellent selectivity and stability as indicated by the above experimental results.

4. Conclusions

In conclusion, the high-entropy $(FeCoNiMnAl)_3O_4$ metal oxide with a microflower shape is successfully fabricated on Ni foam as a highly active electrocatalyst for seawater oxidation through a facile hydrothermal reaction and a sequential calcination process. Excellent OER performance with an overpotential of 274 mV@50 mA cm^{-2} is exhibited in 1 M KOH freshwater based solution. In particular, fairly low overpotentials of 284 and 295 mV are required at 50 mA cm^{-2} even in alkaline simulated and natural seawater based electrolytes, respectively. In addition, this catalyst shows long-time stability for continuous 50-h
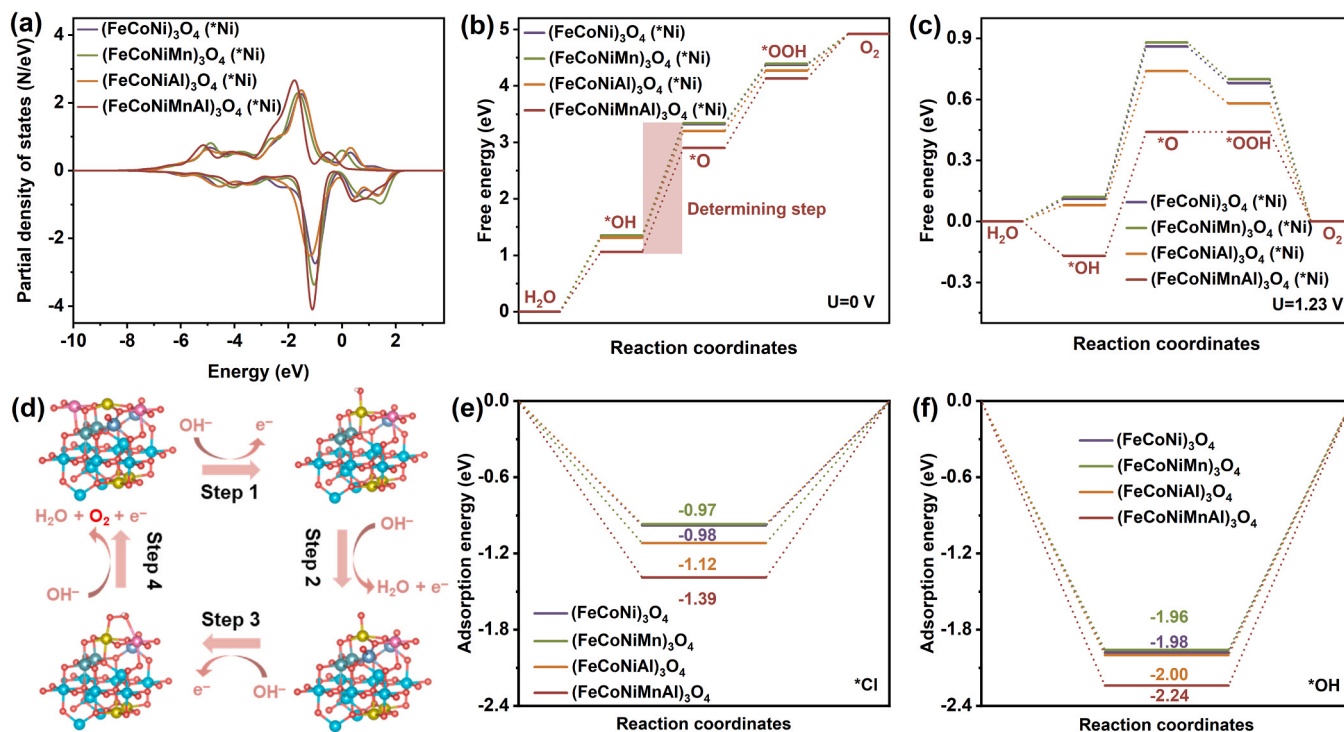

Fig. 6. DFT calculation. (a) *d*-PDOSs of different catalysts; Gibbs free energy diagrams of at (b) U = 0 V and (c) U = 1.23 V; (d) Proposed reaction mechanism of OER on $(FeCoNiMnAl)_3O_4$; Adsorption energy of (e) *Cl and (f) *OH at Ni sites on different catalyst surfaces.

OER at an industrial-level high current density of 500 mA cm^{-2} in alkaline natural seawater, showing promising prospects in industrial applications. The origin of the high OER activity could be attributed to the following factors: (i) the porous 3D microflower shape (FeCo-NiMnAl)$_3$O$_4$ assembled by nanosheets can effectively increase the specific surface area, and the generated cavities in it can further facilitate mass transfer and gas release, resulting in an improved catalytic performance; (ii) the excellent hydrophilicity ensures effective contact of electrocatalysts with the electrolyte, but also is conducive to suppressing the formation of bubbles on the catalyst surface in the electrolysis process, thereby avoiding the gathering of bubbles to cover the active sites and the falling out of catalysts; (iii) rich oxygen vacancies existed in the high-entropy spinel are beneficial to electron transport, leading to positive effect on the electrocatalytic performance; and (iv) DFT calculations verify the strong synergistic effect and stronger adsorption ability for OH$^-$ than Cl$^-$ to ensure excellent OER selectivity of the high-entropy catalyst.

CRediT authorship contribution statement

Changrui Feng: Writing – original draft, Visualization, Validation, Methodology, Investigation, Formal analysis, Data curation, Conceptualization. **Guoqing Guan:** Writing – review & editing, Validation, Supervision, Resources, Project administration, Methodology, Investigation, Funding acquisition, Formal analysis, Data curation, Conceptualization. **Kai Yan:** Writing – review & editing, Validation, Investigation. **Abuliti Abudula:** Writing – review & editing, Supervision, Project administration. **Yifan Zhou:** Investigation. **Lina Zou:** Investigation. **Meng Chen:** Investigation. **Pairuzha Xiaokaiti:** Investigation. **Qiang Zhao:** Investigation. **Xiaowei An:** Validation, Software, Investigation. **Xiumin Li:** Investigation.

Declaration of Competing Interest

The authors declare that they have no known competing financial interests or personal relationships that could have appeared to influence the work reported in this paper.

Data availability

Data will be made available on request.

Appendix A. Supporting information

Supplementary data associated with this article can be found in the online version at doi:10.1016/j.apcatb.2024.123875.

References

[1] A. Ursua, L.M. Gandia, P. Sanchis, Hydrogen production from water electrolysis: current status and future trends, Proc. IEEE Inst. Electr. Electron. Eng. 100 (2012) 410–426.

[2] K. Zeng, D. Zhang, Recent progress in alkaline water electrolysis for hydrogen production and applications, Prog. Energy Combust. Sci. 36 (2010) 307–326.

[3] T. Terlouw, C. Bauer, R. McKenna, M. Mazzotti, Large-scale hydrogen production via water electrolysis: A techno-economic and environmental assessment, Energy Environ. Sci. 15 (2022) 3583–3602.

[4] X. Zou, W. Zhang, X. Zhou, K. Song, X. Ge, W. Zheng, The surface of metal boride tinted by oxygen evolution reaction for enhanced water electrolysis, J. Energy Chem. 72 (2022) 509–515.

[5] M. Elimelech, W.A. Phillip, The future of seawater desalination: energy, technology, and the environment, Science 333 (2011) 712–717.

[6] H. Liu, W. Shen, H. Jin, J. Xu, P. Xi, J. Dong, Y. Zheng, S.-Z. Qiao, High-performance alkaline seawater electrolysis with anomalous chloride promoted oxygen evolution reaction, Angew. Chem. Int. Ed. 62 (2023) e202311674.

[7] S.J. Kim, S.H. Ko, K.H. Kang, J. Han, Direct seawater desalination by ion concentration polarization, Nat. Nanotechnol. 5 (2010) 297–301.

[8] P.R. Buseck, M. Pósfai, Airborne minerals and related aerosol particles: Effects on climate and the environment, Proc. Natl. Acad. Sci. U. S. A. 96 (1999) 3372–3379.

[9] J.G. Vos, T.A. Wezendonk, A.W. Jeremiasse, M.T.M. Koper, MnOx/IrOx as selective oxygen evolution electrocatalyst in acidic chloride solution, J. Am. Chem. Soc. 140 (2018) 10270–10281.

[10] S. Shin, T.-U. Wi, T.-H. Kong, C. Park, H. Lee, J. Jeong, E. Lee, S. Yoon, T.-H. Kim, H.-W. Lee, Y. Kwon, H.-K. Song, Selectively enhanced electrocatalytic oxygen evolution within nanoscopic channels fitting a specific reaction intermediate for seawater splitting, Small 19 (2023) 2206918.

[11] N. Wang, P. Ou, S.F. Hung, J.E. Huang, A. Ozden, J. Abed, I. Grigioni, C. Chen, R. K. Miao, Y. Yan, J. Zhang, Z. Wang, R. Dorakhan, A. Badreldin, A. Abdel-Wahab, D. Sinton, Y. Liu, H. Liang, E.H. Sargent, Strong-proton-adsorption Co-based electrocatalysts achieve active and stable neutral seawater splitting, Adv. Mater. 35 (2023) 2210057.

[12] W. Zang, T. Sun, T. Yang, S. Xi, M. Waqar, Z. Kou, Z. Lyu, Y.P. Feng, J. Wang, S. J. Pennycook, Efficient hydrogen evolution of oxidized Ni-N$_3$ defective sites for alkaline freshwater and seawater electrolysis, Adv. Mater. 33 (2021) 2003846.

[13] S. Zhang, Y. Wang, S. Li, Z. Wang, H. Chen, L. Yi, X. Chen, Q. Yang, X. Xu, A. Wang, Z. Lu, Concerning the stability of seawater electrolysis: a corrosion mechanism study of halide on Ni-based anode, Nat. Commun. 14 (2023) 4822.

[14] B. Zhang, S. Liu, S. Zhang, Y. Cao, H. Wang, C. Han, J. Sun, High corrosion resistance of NiFe-layered double hydroxide catalyst for stable seawater electrolysis promoted by phosphate intercalation, Small 18 (2022) 2203852.

[15] M. Chen, N. Kitiphatpiboon, C. Feng, Q. Zhao, A. Abudula, Y. Ma, K. Yan, G. Guan, Tuning octahedron sites in MnFe$_2$O$_4$ spinel by boron doping for highly efficient seawater splitting, Appl. Catal. B 330 (2023) 122577.

[16] J. Guo, Y. Zheng, Z. Hu, C. Zheng, J. Mao, K. Du, M. Jaroniec, S.-Z. Qiao, T. Ling, Direct seawater electrolysis by adjusting the local reaction environment of a catalyst, Nat. Energy 8 (2023) 264–272.

[17] X. Li, Y. Zhou, C. Feng, R. Wei, X. Hao, K. Tang, G. Guan, High entropy materials based electrocatalysts for water splitting: synthesis strategies, catalytic mechanisms, and prospects, Nano Res. 16 (2023) 4411–4437.

[18] S.K. Nemani, M. Torkamanzadeh, B.C. Wyatt, V. Presser, B. Anasori, Functional two-dimensional high-entropy materials, Commun. Mater. 4 (2023) 16.

[19] L.H. Liu, N. Li, M. Han, J.R. Han, H.Y. Liang, Scalable synthesis of nanoporous high entropy alloys for electrocatalytic oxygen evolution, Rare Met. 41 (2022) 125–131.

[20] Y. Sun, W. Wu, L. Yu, S. Xu, Y. Zhang, L. Yu, B. Xia, S. Ding, M. Li, L. Jiang, J. Duan, J. Zhu, S. Chen, Asymmetric acidic/alkaline N$_2$ electrofixation accelerated by high-entropy metal-organic framework derivatives, Carbon Ener 5 (2023) e263.

[21] Y. Ma, Y. Ma, Q. Wang, S. Schweidler, M. Botros, T. Fu, H. Hahn, T. Brezesinski, B. Breitung, High-entropy energy materials: challenges and new opportunities, Energy Environ. Sci. 14 (2021) 2883–2905.

[22] A. Sarkar, Q. Wang, A. Schiele, M.R. Chellali, S.S. Bhattacharya, D. Wang, T. Brezesinski, H. Hahn, L. Velasco, B. Breitung, High-entropy oxides: fundamental aspects and electrochemical properties, Adv. Mater. 31 (2019) 1806236.

[23] Y. Zhang, T.T. Zuo, Z. Tang, M.C. Gao, K.A. Dahmen, P.K. Liaw, Z.P. Lu, Microstructures and properties of high-entropy alloys, Prog. Mater. Sci. 61 (2014) 1–93.

[24] Y. Xin, S. Li, Y. Qian, W. Zhu, H. Yuan, P. Jiang, R. Guo, L. Wang, High-entropy alloys as a platform for catalysis: Progress, challenges, and opportunities, ACS Catal. 10 (2020) 11280–11306.

[25] K.Y. Tsai, M.H. Tsai, J.W. Yeh, Sluggish diffusion in Co-Cr-Fe-Mn-Ni high-entropy alloys, Acta Mater. 61 (2013) 4887–4897.

[26] Y. Sun, S. Dai, High-entropy materials for catalysis: a new frontier, Sci. Adv. 7 (2021) eabg1600.

[27] S. Yuan, X. Duan, J. Liu, Y. Ye, F. Lv, T. Liu, Q. Wang, X. Zhang, Recent progress on transition metal oxides as advanced materials for energy conversion and storage, Energy Stor. Mater. 42 (2021) 317–369.

[28] Z. Lei, J.M. Lee, G. Singh, C.I. Sathish, X. Chu, Aa.H. Al-Muhtaseb, A. Vinu, J. Yi, Recent advances of layered-transition metal oxides for energy-related applications, Energy Stor. Mater. 36 (2021) 514–550.

[29] Q. Zhao, Z. Yan, C. Chen, J. Chen, Spinels: controlled preparation, oxygen reduction/evolution reaction application, and beyond, Chem. Rev. 117 (2017) 10121–10211.

[30] J. Sun, N. Guo, Z. Shao, K. Huang, Y. Li, F. He, Q. Wang, A Facile strategy to construct amorphous spinel-based electrocatalysts with massive oxygen vacancies using ionic liquid dopant, Adv. Energy Mater. 8 (2018) 1800980.

[31] D. Wang, Y. Chen, L. Fan, T. Xiao, T. Meng, Z. Xing, X. Yang, Bulk and surface dual modification of nickel-cobalt spinel with ruthenium toward highly efficient overall water splitting, Appl. Catal. B 305 (2022) 121081.

[32] J. Li, T. Hu, C. Wang, C. Guo, Surface-mediated iron on porous cobalt oxide with high energy state for efficient water oxidation electrocatalysis, Green. Energ. Environ. 7 (2022) 662–671.

[33] Y. Zhou, S. Sun, C. Wei, Y. Sun, P. Xi, Z. Feng, Z.J. Xu, Significance of engineering the octahedral units to promote the oxygen evolution reaction of spinel oxides, Adv. Mater. 31 (2019) 1902509.

[34] W. Wang, Z. Wang, Y. Hu, Y. Liu, S. Chen, A potential-driven switch of activity promotion mode for the oxygen evolution reaction at Co_3O_4/NiO_xH_y interface, eScience 2 (2022) 438–444.

[35] L. Li, X. Cao, J. Huo, J. Qu, W. Chen, C. Liu, Y. Zhao, H. Liu, G. Wang, High valence metals engineering strategies of Fe/Co/Ni-based catalysts for boosted OER electrocatalysis, J. Energy Chem. 76 (2023) 195–213.

[36] P. Wu, S. Cheng, M. Yao, L. Yang, Y. Zhu, P. Liu, O. Xing, J. Zhou, M. Wang, H. Luo, M. Liu, A low-cost, self-standing $NiCo_2O_4$@CNT/CNT multilayer electrode for flexible asymmetric solid-state supercapacitors, Adv. Funct. Mater. 27 (2017) 1702160.

[37] C. Triolo, M. Maisuradze, M. Li, Y. Liu, A. Ponti, G. Pagot, V. Di Noto, G. Aquilanti, N. Pinna, M. Giorgetti, S. Santangelo, Charge storage mechanism in electrospun spinel-structured high-entropy $(Mn_{0.2}Fe_{0.2}Co_{0.2}Ni_{0.2}Zn_{0.2})_3O_4$ oxide nanofibers as anode material for Li-ion batteries, Small 19 (2023) 2304585.

[38] L. Xiang, D. Jiang, Y. Gao, C. Zhang, X. Ren, L. Zhu, S. Gao, X. Zhan, Self-formed fluorinated interphase with Fe valence gradient for dendrite-free solid-state sodium-metal batteries, Adv. Funct. Mater. (2023) 2301670.

[39] Z. Liu, H. Tan, D. Liu, X. Liu, J. Xin, J. Xie, M. Zhao, L. Song, L. Dai, H. Liu, Promotion of overall water splitting activity over a wide pH range by interfacial electrical effects of metallic NiCo-nitrides nanoparticle/$NiCo_2O_4$ nanoflake/graphite fibers, Adv. Sci. 6 (2019) 1801829.

[40] J. Yan, L. Chen, X. Liang, Co_9S_8 nanowires@NiCo LDH nanosheets arrays on nickel foams towards efficient overall water splitting, Sci. Bull. 64 (2019) 158–165.

[41] P. Plate, C. Höhn, U. Bloeck, P. Bogdanoff, S. Fiechter, F.F. Abdi, R. van de Krol, A. C. Bronneberg, On the origin of the OER activity of ultrathin manganese oxide films, ACS Appl. Mater. Interfaces 13 (2021) 2428–2436.

[42] L. Yan, Y. Ren, X. Zhang, Y. Sun, J. Ning, Y. Zhong, B. Teng, Y. Hu, Electronic modulation of composite electrocatalysts derived from layered NiFeMn triple hydroxide nanosheets for boosted overall water splitting, Nanoscale 11 (2019) 20797–20808.

[43] L.Q. Zhu, Y.H. Liu, H.L. Zhang, H. Xiao, L.Q. Guo, Atomic layer deposited Al_2O_3 films for anti-reflectance and surface passivation applications, Appl. Surf. Sci. 288 (2014) 430–434.

[44] Y. Zhu, L. Zhang, B. Zhao, H. Chen, X. Liu, R. Zhao, X. Wang, J. Liu, Y. Chen, M. Liu, Improving the activity for oxygen evolution reaction by tailoring oxygen defects in double perovskite oxides, Adv. Funct. Mater. 29 (2019) 1901783.

[45] S. Sun, T. Zhai, C. Liang, S.V. Savilov, H. Xia, Boosted crystalline/amorphous $Fe_2O_{3-\delta}$ core/shell heterostructure for flexible solid-state pseudocapacitors in large scale, Nano Energy 45 (2018) 390–397.

[46] Z. Xiao, Y.-C. Huang, C.-L. Dong, C. Xie, Z. Liu, S. Du, W. Chen, D. Yan, L. Tao, Z. Shu, G. Zhang, H. Duan, Y. Wang, Y. Zou, R. Chen, S. Wang, Operando Identification of the dynamic behavior of oxygen vacancy-rich Co_3O_4 for oxygen evolution reaction, J. Am. Chem. Soc. 142 (2020) 12087–12095.

[47] P. Li, S. Zhao, Y. Huang, Q. Huang, B. Xi, X. An, S. Xiong, Corrosion resistant multilayered electrode comprising Ni_3N nanoarray overcoated with NiFe-Phytate complex for boosted oxygen evolution in seawater electrolysis, Adv. Energy Mater. (2023) 2303360.

[48] N. Bastan, M. Ahmadi, T. Madrakian, A. Afkhami, S. Khalili, M. Majidi, M. Moradi, A paired emitter-detector diode-based photometer for the determination of sodium hypochlorite adulteration in milk, Sci. Rep. 13 (2023) 6217.

[49] L. Cai, Y. Liu, J. Zhang, Q. Jia, J. Guan, H. Sun, Y. Yu, Y. Huang, Unveiling the geometric site dependent activity of spinel Co_3O_4 for electrocatalytic chlorine evolution reaction, J. Energy Chem. (2023), https://doi.org/10.1016/j.jechem.2023.12.002.

[50] Y. Wu, C. Li, W. Liu, H. Li, Y. Gong, L. Niu, X. Liu, C. Sun, S. Xu, Unexpected monoatomic catalytic-host synergetic OER/ORR by graphitic carbon nitride: density functional theory, Nanoscale 11 (2019) 5064–5071.

[51] C. Huang, Q. Zhou, L. Yu, D. Duan, T. Cao, S. Qiu, Z. Wang, J. Guo, J. Xie, L. Li, Y. Yu, Functional bimetal co-modification for boosting large-current-density seawater electrolysis by inhibiting adsorption of chloride ions, Adv. Energy Mater. 13 (2023) 2301475.